An Advanced Interferometric Baseline Estimation Method (IBEM) for Spaceborne Bistatic SAR

Yanyan Zhang, *Member, IEEE*, Junfeng Li, Pingping Lu, *Member, IEEE*, and Robert Wang, *Senior Member, IEEE*

***Abstract*—Spaceborne bistatic synthetic aperture radar (BiSAR) employs single-pass cross-track interferometry (XTI) to invert digital elevation models (DEMs) of target areas. However, the accuracy of the inverted DEM is affected by various factors, especially interferometric baseline estimation. To this end, this article proposes an advanced interferometric baseline estimation method (IBEM) for spaceborne BiSAR. First, the IBEM compensates for the time synchronization deviation of BiSAR systems using the pulse exchange phase synchronization method. Subsequently, the time, position, and velocity vectors of satellites are input into a high-precision orbit propagator to derive the state vectors at the imaging time. Leveraging these state vectors, the interferometric baseline is calculated with the main satellite that transmits radar signals as the origin of the coordinate system. Eventually, interferometric baseline estimation and DEM generation are performed based on two sets of data from the LuTan-1 (LT-1) BiSAR system, and the generated DEMs are compared with the external reference DEM to evaluate the performance of the IBEM and the LT-1 system. Results indicate that the proposed IBEM can accurately estimate the interferometric baseline and has extensive application prospects in future spaceborne multibaseline Interferometric SAR missions.**

***Index Terms*—Baseline estimation, bistatic synthetic aperture radar (SAR), cross-track interferometry (XTI), LuTan-1(LT-1).**

I. Introduction

SPACEBORNE bistatic SAR (BiSAR) refers to a single-pass distributed microwave imaging system, and it consists of a spatially separated transmitter and receiver [1], [2], [3]. BiSAR can obtain multidimensional scattering information of target areas through multiangle imaging. It has extensive application prospects, such as moving target detection, surface subsidence measurement, high-resolution and wide-swath imaging, natural disaster monitoring, and digital elevation model (DEM) generation [4]. High-precision DEM provides scientific evidence for road planning and dam site selection. Moreover, DEM can be used to calculate slope maps and slope profiles and to help analyze geomorphology and estimate erosion [4], [5]. As such, high-precision DEM generation is an important topic.

The DEM can be generated by the classical interferometric SAR (InSAR) technology [7]. InSAR can be achieved by the repeat-pass interferometry of monostatic SAR or single-pass interferometry of distributed SAR, and the latter is the focus. First, two satellites flying in close formation separated along the range direction observe the same target area and obtain two single look complex (SLC) images. Afterward, the two SLC images are registered and cross-correlated to obtain an interferogram. Finally, a high-precision DEM of the target area can be generated according to the classical DEM generation procedure [7].

Driven by application requirements, several distributed SAR systems were launched one after another. In 2007 and 2010, the German Aerospace Center (DLR) launched TSX and TDX SAR satellites respectively, forming the X-band bistatic InSAR system TanDEM-X [8], [9]. In early 2022, China launched the LuTan-1 (LT-1) SAR satellites, forming an L-band BiSAR system [6], [10], as shown in Fig. 1. At present, the LT-1 system has completed commissioning and put into use, and it is detailed in Section II. In 2023, the first commercially distributed SAR system HongTu-1 (PIESAT-1, i.e., Nuwa-1) was launched [11]. The HongTu-1 is composed of four SAR satellites that inherit the clock synchronization method and imaging mode of the LT-1, and the four SAR satellites fly in close formation with the Cartwheel configuration to form an X-band single-pass multibaseline InSAR system [11], [12]. Meanwhile, some distributed SAR concepts were put forward [13], [14], [15], [16]. Since 2017, Krieger et al. proposed the MirrorSAR concept, the Double-MirrorLink phase synchronization method, and the system design method [13], [16]. In 2019, Lopez-Dekker et al. [14] presented the distributed SAR concept of Harmony and discussed its mission planning. In 2021, Zhang et al. [12], [15] put forward the Superpolyhedron satellite formation and the Push-To-Talk clock synchronization method for spaceborne multibaseline InSAR. In short, the endless emergence of distributed SAR missions has paved the way to obtain high-precision DEM.

The high-precision DEM generation is affected by various factors, such as interferometric baseline estimation [17]. The

Manuscript received 27 November 2023; revised 13 February 2024 and 18 March 2024; accepted 7 May 2024. Date of publication 10 May 2024; date of current version 23 May 2024. This work was supported in part by the Medium- and Long-Term Development Plan for China's Civil Space Infrastructure, LuTan-1 (LT-1), and in part by the China Scholarship Council under Grant 202102527023. *(Corresponding authors: Pingping Lu; Yanyan Zhang.)*

Yanyan Zhang is with the National Key Laboratory of Microwave Imaging Technology, Aerospace Information Research Institute, Chinese Academy of Sciences, Beijing 100190, China, and also with the Department of Civil, Environmental and Geomatic Engineering, ETH Zürich, 8093 Zürich, Switzerland (e-mail: yanyzhang@ethz.ch).

Junfeng Li, Pingping Lu, and Robert Wang are with the National Key Laboratory of Microwave Imaging Technology, Aerospace Information Research Institute, Chinese Academy of Sciences, Beijing 100190, China, and also with the School of Electronic, Electrical and Communication Engineering, University of Chinese Academy of Sciences, Beijing 100049, China (e-mail: lijunfeng201@mails.ucas.ac.cn; lupp@aircas.ac.cn; yuwang@mail.ie.ac.cn).

Digital Object Identifier 10.1109/JSTARS.2024.3399321

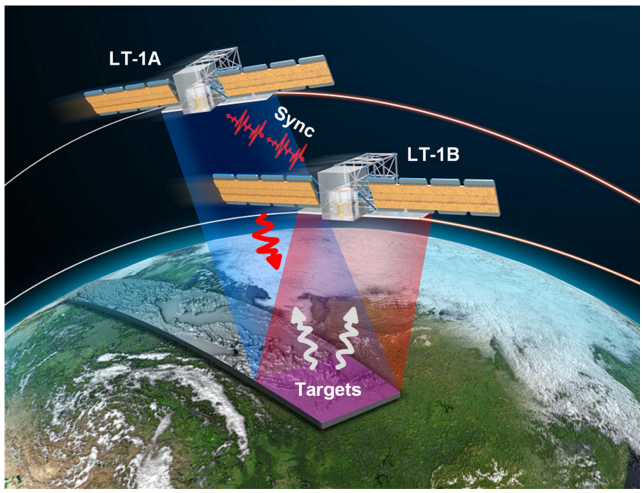

Fig. 1. It is an imaging diagram of the LuTan-1 (LT-1) system. One satellite (e.g., LT-1 A) transmits a radar signal to illuminate the target area, and two satellites receive the echo signal. At the same time, the LT-1 uses the noninterrupted pulse exchange phase synchronization method to achieve clock synchronization [6].

interferometric baseline refers to the vector from the antenna phase center of the main satellite to the antenna phase center of the slave satellite when the two SAR satellites illuminate the same target area. It should be noted that the main satellite is the platform that transmits radar signals and the slave satellite is the platform that receives echo signals. The estimation error of interferometric baselines leads to the flat phase error and a coefficient error in the conversion of the topographic phase to elevation, significantly reducing the DEM accuracy [17]. Thus, baseline estimation is a major step in achieving high-precision DEM generation.

Baseline estimation of InSAR usually adopts methods based on images and methods based on external data. The first type of method usually estimates interferometric baselines according to the relationship between the interferometric baseline and the registration offset or frequency fringes of the interferogram [18], [19]. They require no extra information other than some high-quality SAR images. Nevertheless, additional parameters need to be selected in the calculation process, resulting in baseline estimation errors. The second type of method usually requires ground control points (GCPs) or external DEM [20], [21], [22], and the GCPs-based method achieves baseline estimation by establishing an interferometric observation equation and combining GCPs to calculate the solution of the equation. The estimation accuracy of the GCPs-based method is accurate. However, the high-precision GCPs in the target area are difficult to obtain. The DEM-based method calculates the residual phase between the interferometric phase simulated by external DEM and the interferometric phase of processed data and constructs an interferometric observation equation based on the relationship between the baseline and the residual phase to achieve baseline estimation. These methods require high-quality images or external data. Besides, their estimation accuracy is easily affected by system noise and ambiguities, and the calculation is complicated [22]. It should be mentioned that the LiDAR-based elevation and the methods based on external data can be used to correct interferometric baselines, and the additional LiDAR increases the system cost. The LuTan-1 (LT-1) system does not take extra sensors, and baseline estimation based on satellite orbital parameters is a major candidate.

To more fully evaluate the performance of InSAR systems, various systematic errors should be estimated and compensated separately. However, these methods [18], [19], [20], [21], [22] treat other errors as baseline errors, and the baseline is incorrectly corrected, as discussed in Section V. In other words, the inverted DEM by these methods can not be used to evaluate the performance of the InSAR system. To avoid correcting other systematic errors to baseline errors resulting in incorrect system evaluation, this article, based on satellite orbital parameters,[1] puts forward an advanced interferometric baseline estimation method (IBEM). It should be noted that the time synchronization deviation of BiSAR causes errors in the calculation of satellite positions, which in turn leads to baseline errors. As such, time deviations should be compensated first. The TanDEM-X adopts the GPS signals to trigger its startup time, and then its system time is controlled with a high-stable clock source [23]. Different from the TanDEM-X, the LT-1 uses a pulse-per-second pulse of the GPS to synchronize time, and the GPS-disciplined clock [24] is used to maintain the time synchronization. Based on the processing framework of the LT-1 [25], time deviations can be estimated from the synchronization signals, and the influence of time deviations can be removed in baseline estimation, as detailed in Section III. Subsequently, the time, position, and velocity vectors of satellites after time deviation compensation are input into a high-precision orbit propagator [26], and the state vectors at the imaging time can be derived. Afterward, the interferometric baseline can be estimated based on the derived state vectors. Finally, interferometric baseline estimation and DEM generation are performed based on the LT-1 data, and the results are compared with the external reference DEM to evaluate the performance of the IBEM and the LT-1 system.

The rest of this article is organized as follows. Section II introduces the single-pass interferometry of the LT-1, including satellite formation and DEM generation. Section III details the basic principles and processing procedure of the proposed IBEM. Section IV performs interferometric baseline estimation and DEM generation based on the IBEM and the LT-1 data and evaluates the DEM accuracy and the performance of the IBEM. Section V discusses the accuracy of the IBEM. Finally, Section VI concludes this article.

II. L-Band BiSAR Mission

The LT-1 was established in November 2016, and its main system parameters and indicators are shown in Table I. It was the first satellite in the Medium- and Long-Term Development Plan of China's Civil Space Infrastructure from 2015 to 2025, and it is the first Earth observation radar satellite with the main task

[1] It is noted that baseline estimation based on satellite orbital parameters avoids correcting other errors as baseline errors, as discussed in Section V.

TABLE I
MAIN PARAMETERS OF THE LT-1 MISSION

Parameters	Values
Orbit height	607 km
Orbit inclination	97.8 deg
Antenna Size (Length/Height)	9.8 m/3.4 m
Carrier frequency	1.26 GHz
Azimuth resolution	3 m
Radar signal bandwidth	80 MHz
Radar signal duration	100 us
Synchronization signal bandwidth	80 MHz
Synchronization signal duration	10 us
Operating life	8 years
Polarization mode	Single/Double/Quad/Compact
Relative DEM accuracy	5 m
Absolute DEM accuracy	10 m
Spatial resolution	12 m (4 looks)

of monitoring surface subsidence. After launching, it has served several industries, such as earthquake, environment, surveying and mapping, and forestry [27], [28].

The LT-1 is composed of two L-band full-polarization multichannel SAR satellites and has flexible formation flight capabilities, as shown in Fig. 1 [29]. The main satellite transmits a radar signal to illuminate the target area, and the two satellites receive the radar echoes. Since it adopts the single-transmit and dual-receive imaging mode, the LT-1 system can avoid the impact of time decorrelation and atmospheric disturbance on the interferometric phase [29], which improves the InSAR performance.

A. Satellite Formation

The LT-1 [6] adopts the Helix formation to achieve single-pass cross-track interferometry (XTI), and it has very flexible baseline adjustment capabilities. This enables the interferometric baseline of the LT-1 to adapt to complex observation terrains. Since the baseline length provided by a set of orbital parameters cannot meet the requirements for interferometry in a wide-latitude area, the LT-1 uses high- and low-orbital parameters to observe high- and low-latitude areas, respectively [6]. A diagram of interferometric baseline variations corresponding to the two sets of orbital parameters within one orbital period is shown in Fig. 2.

It should be noted that the high and low orbital parameters can be obtained by fine-tuning the eccentricity, the argument of perigee, the right ascension of the ascending node, and the initial mean anomaly of the satellite orbit, for details see [6]. Besides, the LT-1 adopted the first and second sets of orbital parameters before September and after October 2022 respectively, and it has observed a large area of the Earth.

B. DEM Generation

The LT-1 acquired a large amount of BiSAR data with the Helix formation. Furthermore, InSAR processing is performed based on the data to obtain high-precision DEM products and evaluate the LT-1 system performance. A classical procedure for the DEM generation of the LT-1 is shown in Fig. 3.

First, the two SAR images are registered according to the criterion of coherence and external DEM, and an interferogram is generated. Second, the flat and topographic phases of the interferogram are removed based on the external DEM (e.g., the SRTM), and the minimum cost flow method is used for phase unwrapping. Then, the flat and topographic phases are added to the unwrapped phase, which is defaulted here. Moreover, the interferometric baseline is estimated according to the registration offsets or satellite orbital parameters. Meanwhile, the baseline error can be compensated based on interferometric calibration fields, and absolute phase estimation and compensation are performed. Eventually, a high-precision DEM of the target area can be inverted by the conversion of the topographic phase to elevation [7]. It is noted that the absolute phase offset is estimated by the radargrammetric method in [30] and [31], the slant range deviation resulting from the system circuit delay is estimated based on the calibration field, and the slant range deviation has been compensated during the imaging process.

Baseline estimation based on satellite orbital parameters is the focus here. Thus, to evaluate the estimation accuracy of the baselines, the interferometric calibration is not used to correct the estimated baseline in the subsequent data processing, and the proposed IBEM is introduced as follows.

III. INTERFEROMETRIC BASELINE ESTIMATION METHOD (IBEM)

To accurately estimate the XTI baseline of the LT-1 system and improve DEM accuracy, this article proposes an advanced IBEM for BiSAR. The IBEM mainly includes three segments, as shown in Fig. 4. First, the time synchronization deviation of the two satellites is compensated based on the pulse exchange phase synchronization method. After that, based on the high-precision orbit propagator and satellite orbital parameters, the state vectors at the imaging time are derived. Finally, the XTI baseline is calculated with the main satellite as the origin of the coordinate system.

A. Compensation for Time Synchronization Deviations

LT-1 A and LT-1B adopt different GPS-disciplined rubidium clocks to generate reference time signals. Therefore, it can be assumed that the azimuth times of the main satellite and the slave satellite are, respectively,

$$\mathrm{t_{M,i}} = t_{M,0} + (i-1)\cdot \mathrm{PRT_M} \tag{1}$$

$$\mathrm{t_{S,j}} = t_{S,0} + (j-1)\cdot \mathrm{PRT_S} \tag{2}$$

where the subscripts M and S, respectively, represent the main satellite and the slave satellite, $\mathrm{t_{M,0}}$ is the start time of the main satellite imaging, $\mathrm{t_{S,0}}$ is the start time of the slave satellite imaging, i is the ith pulse repetition time (PRT) of the main satellite,

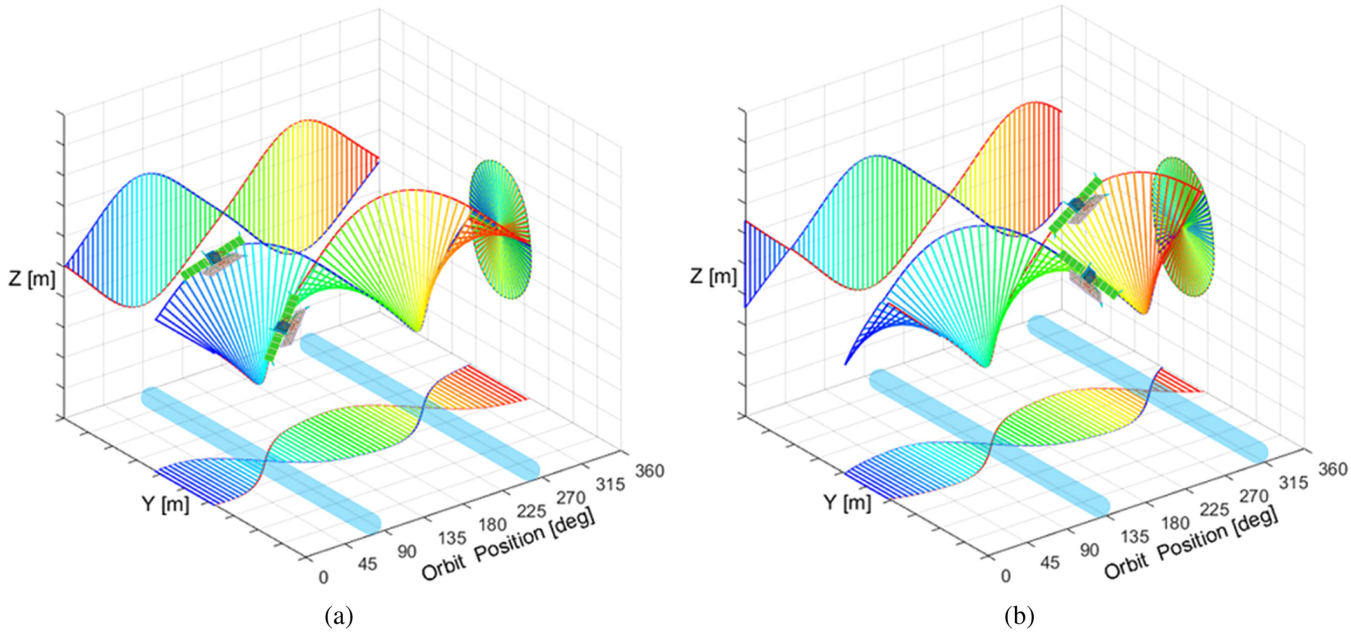

Fig. 2. Interferometric baseline variations correspond to the two sets of orbital parameters within one orbital period, and the blue part on the bottom indicates the area where the baseline length does not meet the requirements of XTI [6]. (a) Interferometric baseline of high orbital parameters. (b) interferometric baseline of low orbital parameters.

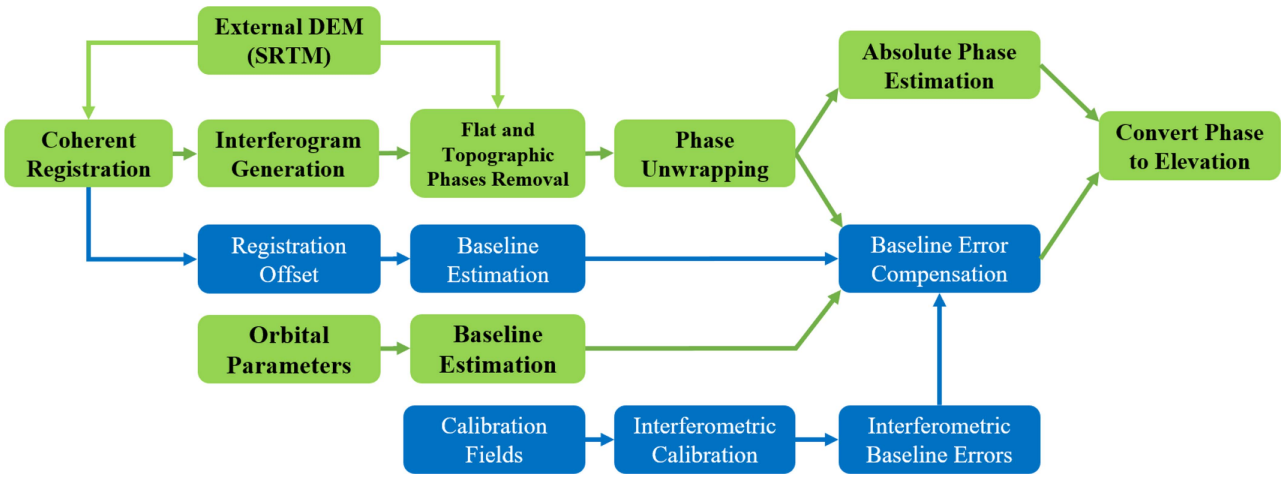

Fig. 3. Classical procedure for generating DEM.

$\mathrm{i} \in \{1, 2, \ldots, \mathrm{N_M}\}$, $\mathrm{N_M}$ is the number of PRTs on the main satellite, j is the jth PRT of the slave satellite, $\mathrm{j} \in \{1, 2, \ldots, \mathrm{N_S}\}$, $\mathrm{N_S}$ is the number of PRTs on the slave satellite, $\mathrm{PRT_M}$ is the PRT of the main satellite, $\mathrm{PRT_S}$ is the PRT of the slave satellite, and $\mathrm{PRT_M} \approx \mathrm{PRT_S} \approx \mathrm{PRT}$.

The LT-1 system adopts the noninterrupted pulse exchange phase synchronization method to obtain the time deviation of satellites without affecting the normal radar operation [25], [32]. First, the main satellite transmits a synchronization signal to the slave satellite during the free duration of the first PRT except for the transmitting and echo receiving windows. Second, the slave satellite transmits a synchronization signal to the main satellite during the same free duration in the second PRT. After that, the two satellites alternately transmit synchronization signals to each other, and the synchronization data are downloaded to the receiving station. Moreover, the time corresponding to the peak position of the pulse-compressed synchronization signal of the main satellite is subtracted from the time corresponding to the peak position of the pulse-compressed synchronization signal of the slave satellite to obtain the time difference, and the details are described in [25]. Then, the time difference is divided by 2, and the time deviation $\Delta \mathrm{t} = \mathrm{t_{S,0}} - \mathrm{t_{M,0}}$ of satellites can be calculated. Finally, the azimuth time of the slave satellite is shifted $\Delta \mathrm{t}$ to the right, and the synchronized azimuth time of the slave satellite can be described as

$$\hat{\mathrm{t}}_{\mathrm{S,j}} = \mathrm{t_{S,j}} - \Delta \mathrm{t} = \mathrm{t_{M,0}} + (\mathrm{j} - 1) \cdot \mathrm{PRT}. \tag{3}$$

TABLE II
MODEL OF A HIGH-PRECISION ORBIT PROPAGATOR [12], [26]

Type	Model
Geopotential	EGM96
Atmospheric drag	A dynamical atmospherical density model, such as the Jacchia–Roberts model
SRP	A spherical shape model and a dual-cone shadow model
Celestial acceleration	Lunisolar attraction
Other perturbations	Solid tides and other minor perturbations (e.g., general relativity)

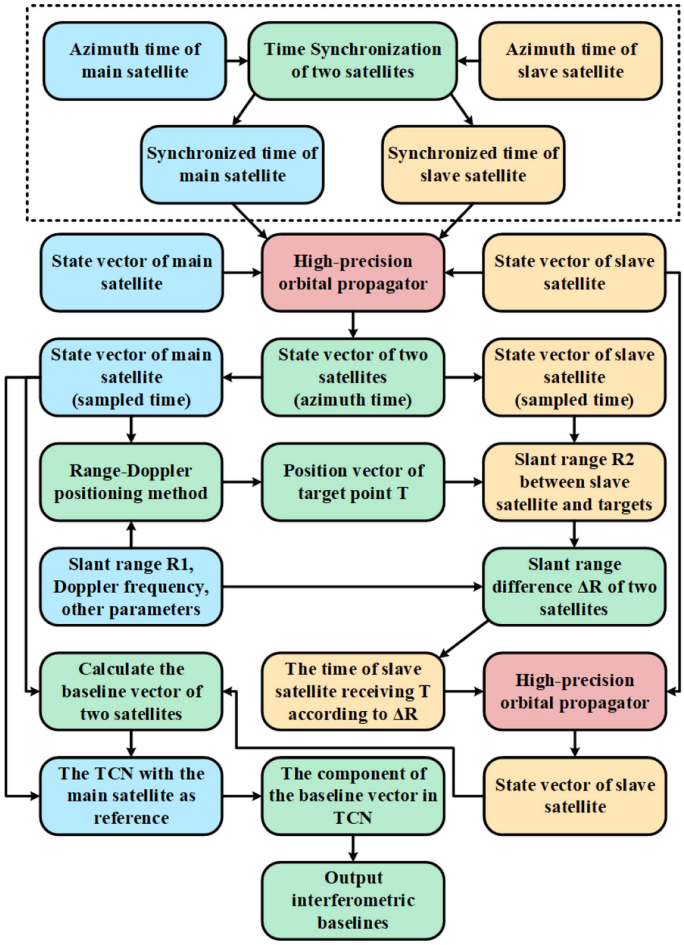

Fig. 4. Main procedure of an IBEM for spaceborne BiSAR.

For convenience of description, the synchronized azimuth time of the main satellite is recast as

$$\hat{t}_{M,i} = t_{M,i} = t_{M,0} + (i-1)\cdot PRT. \tag{4}$$

B. State Vector Generation At the Imaging Time

In Fig. 4, the position vector and velocity vector of satellites at the imaging time are obtained based on the synchronized azimuth time, satellite orbital parameters, and the high-precision orbit propagator in Table II [26], and it is detailed as follows.

First, it can be assumed that the second-interval sampling time vector, position vector, and velocity vector of the GPS of the main satellite are $\mathbf{T_M}$, $\mathbf{P_M}$, and $\mathbf{V_M}$, respectively, and the second-interval sampling time vector, position vector, and velocity vector of the GPS of the slave satellite are $\mathbf{T_S}$, $\mathbf{P_S}$, and $\mathbf{V_S}$, respectively. At this time, the second-interval sampling time vectors of the main satellite and the slave satellite can be, respectively, represented as

$$\mathbf{T_M} = [T_{M,1}, \ldots, T_{M,p}, \ldots, T_{M,P}] \tag{5}$$

$$\mathbf{T_S} = [T_{S,1}, \ldots, T_{S,a}, \ldots, T_{S,A}] \tag{6}$$

where $T_{M,p} - T_{M,p-1} = 1$, $T_{S,a} - T_{S,a-1} = 1$, $T_{M,1} < \hat{t}_{M,1}$, $T_{M,P} > \hat{t}_{M,N_M}$, $T_{S,1} < \hat{t}_{S,1}$, $T_{S,A} > \hat{t}_{S,N_S}$, and P and A denote the number of second-interval samples of the main satellite and the slave satellite, respectively.

The position vector and velocity vector of the main satellite are, respectively, described as

$$\mathbf{P_M} = \begin{bmatrix} P_{M,1,X} & \cdots & P_{M,P,X} \\ P_{M,1,Y} & \cdots & P_{M,P,Y} \\ P_{M,1,Z} & \cdots & P_{M,P,Z} \end{bmatrix} \tag{7}$$

$$\mathbf{V_M} = \begin{bmatrix} V_{M,1,X} & \cdots & V_{M,P,X} \\ V_{M,1,Y} & \cdots & V_{M,P,Y} \\ V_{M,1,Z} & \cdots & V_{M,P,Z} \end{bmatrix}. \tag{8}$$

Similarly, the position vector and velocity vector of the slave satellite are, respectively, expressed as

$$\mathbf{P_S} = \begin{bmatrix} P_{S,1,X} & \cdots & P_{S,A,X} \\ P_{S,1,Y} & \cdots & P_{S,A,Y} \\ P_{S,1,Z} & \cdots & P_{S,A,Z} \end{bmatrix} \tag{9}$$

$$\mathbf{V_S} = \begin{bmatrix} V_{S,1,X} & \cdots & V_{S,A,X} \\ V_{S,1,Y} & \cdots & V_{S,A,Y} \\ V_{S,1,Z} & \cdots & V_{S,A,Z} \end{bmatrix}. \tag{10}$$

Then, the synchronized azimuth time $\left(\hat{t}_{M,i} \text{ and } \hat{t}_{S,j}\right)$ of the two satellites, $\mathbf{T_M}$, $\mathbf{P_M}$, and $\mathbf{V_M}$ of the main satellite, and $\mathbf{T_S}$, $\mathbf{P_S}$, and $\mathbf{V_S}$ of the slave satellite are input into the high-precision orbit propagator to generate the synchronized time vector, position vector, and velocity vector of the two satellites, and they are, respectively, described as

$$\hat{\mathbf{T}}_\mathbf{M} = [\hat{t}_{M,1}, \ldots, \hat{t}_{M,i}, \ldots, \hat{t}_{M,N_M}] \tag{11}$$

$$\hat{\mathbf{P}}_\mathbf{M} = \begin{bmatrix} \hat{P}_{M,1,X} & \cdots & \hat{P}_{M,N_M,X} \\ \hat{P}_{M,1,Y} & \cdots & \hat{P}_{M,N_M,Y} \\ \hat{P}_{M,1,Z} & \cdots & \hat{P}_{M,N_M,Z} \end{bmatrix} \tag{12}$$

$$\hat{\mathbf{V}}_{\mathbf{M}} = \begin{bmatrix} \hat{\mathrm{V}}_{\mathrm{M},1,\mathrm{X}} & \cdots & \hat{\mathrm{V}}_{\mathrm{M},\mathrm{N_M},\mathrm{X}} \\ \hat{\mathrm{V}}_{\mathrm{M},1,\mathrm{Y}} & \cdots & \hat{\mathrm{V}}_{\mathrm{M},\mathrm{N_M},\mathrm{Y}} \\ \hat{\mathrm{V}}_{\mathrm{M},1,\mathrm{Z}} & \cdots & \hat{\mathrm{V}}_{\mathrm{M},\mathrm{N_M},\mathrm{Z}} \end{bmatrix} \tag{13}$$

$$\hat{\mathbf{T}}_{\mathbf{S}} = [\hat{\mathrm{t}}_{\mathrm{S},1}, \ldots, \hat{\mathrm{t}}_{\mathrm{S,j}}, \ldots, \hat{\mathrm{t}}_{\mathrm{S},\mathrm{N_S}}] \tag{14}$$

$$\hat{\mathbf{P}}_{\mathbf{S}} = \begin{bmatrix} \hat{\mathrm{P}}_{\mathrm{S},1,\mathrm{X}} & \cdots & \hat{\mathrm{P}}_{\mathrm{S},\mathrm{N_S},\mathrm{X}} \\ \hat{\mathrm{P}}_{\mathrm{S},1,\mathrm{Y}} & \cdots & \hat{\mathrm{P}}_{\mathrm{S},\mathrm{N_S},\mathrm{Y}} \\ \hat{\mathrm{P}}_{\mathrm{S},1,\mathrm{Z}} & \cdots & \hat{\mathrm{P}}_{\mathrm{S},\mathrm{N_S},\mathrm{Z}} \end{bmatrix} \tag{15}$$

$$\hat{\mathbf{V}}_{\mathbf{S}} = \begin{bmatrix} \hat{\mathrm{V}}_{\mathrm{S},1,\mathrm{X}} & \cdots & \hat{\mathrm{V}}_{\mathrm{S},\mathrm{N_S},\mathrm{X}} \\ \hat{\mathrm{V}}_{\mathrm{S},1,\mathrm{Y}} & \cdots & \hat{\mathrm{V}}_{\mathrm{S},\mathrm{N_S},\mathrm{Y}} \\ \hat{\mathrm{V}}_{\mathrm{S},1,\mathrm{Z}} & \cdots & \hat{\mathrm{V}}_{\mathrm{S},\mathrm{N_S},\mathrm{Z}} \end{bmatrix}. \tag{16}$$

After that, the synchronized time vector of the main satellite is sampled every N interval ($\mathrm{N} \in \mathrm{N}+$) along the azimuth time, and the sampled time vector, position vector, and velocity vector of the main satellite are obtained, and they are, respectively, expressed as

$$\widetilde{\mathbf{T}}_{\mathbf{M}} = [\hat{\mathrm{t}}_{\mathrm{M},1}, \hat{\mathrm{t}}_{\mathrm{M},1+\mathrm{N}}, \cdots] \tag{17}$$

$$\widetilde{\mathbf{P}}_{\mathbf{M}} = \begin{bmatrix} \hat{\mathrm{P}}_{\mathrm{M},1,\mathrm{X}} & \hat{\mathrm{P}}_{\mathrm{M},1+\mathrm{N},\mathrm{X}} & \cdots \\ \hat{\mathrm{P}}_{\mathrm{M},1,\mathrm{Y}} & \hat{\mathrm{P}}_{\mathrm{M},1+\mathrm{N},\mathrm{Y}} & \cdots \\ \hat{\mathrm{P}}_{\mathrm{M},1,\mathrm{Z}} & \hat{\mathrm{P}}_{\mathrm{M},1+\mathrm{N},\mathrm{Z}} & \cdots \end{bmatrix} \tag{18}$$

$$\widetilde{\mathbf{V}}_{\mathbf{M}} = \begin{bmatrix} \hat{\mathrm{V}}_{\mathrm{M},1,\mathrm{X}} & \hat{\mathrm{V}}_{\mathrm{M},1+\mathrm{N},\mathrm{X}} & \cdots \\ \hat{\mathrm{V}}_{\mathrm{M},1,\mathrm{Y}} & \hat{\mathrm{V}}_{\mathrm{M},1+\mathrm{N},\mathrm{Y}} & \cdots \\ \hat{\mathrm{V}}_{\mathrm{M},1,\mathrm{Z}} & \hat{\mathrm{V}}_{\mathrm{M},1+\mathrm{N},\mathrm{Z}} & \cdots \end{bmatrix}. \tag{19}$$

Based on the sampled time vector of the main satellite, the state vector of the slave satellite with the same synchronized time is extracted. Afterward, the sampled time vector, position vector, and velocity vector of the slave satellite can be obtained as

$$\widetilde{\mathbf{T}}_{\mathbf{S}} = [\hat{\mathrm{t}}_{\mathrm{S},1}, \hat{\mathrm{t}}_{\mathrm{S},1+\mathrm{N}}, \cdots] \tag{20}$$

$$\widetilde{\mathbf{P}}_{\mathbf{S}} = \begin{bmatrix} \hat{\mathrm{P}}_{\mathrm{S},1,\mathrm{X}} & \hat{\mathrm{P}}_{\mathrm{S},1+\mathrm{N},\mathrm{X}} & \cdots \\ \hat{\mathrm{P}}_{\mathrm{S},1,\mathrm{Y}} & \hat{\mathrm{P}}_{\mathrm{S},1+\mathrm{N},\mathrm{Y}} & \cdots \\ \hat{\mathrm{P}}_{\mathrm{S},1,\mathrm{Z}} & \hat{\mathrm{P}}_{\mathrm{S},1+\mathrm{N},\mathrm{Z}} & \cdots \end{bmatrix} \tag{21}$$

$$\widetilde{\mathbf{V}}_{\mathbf{S}} = \begin{bmatrix} \hat{\mathrm{V}}_{\mathrm{S},1,\mathrm{X}} & \hat{\mathrm{V}}_{\mathrm{S},1+\mathrm{N},\mathrm{X}} & \cdots \\ \hat{\mathrm{V}}_{\mathrm{S},1,\mathrm{Y}} & \hat{\mathrm{V}}_{\mathrm{S},1+\mathrm{N},\mathrm{Y}} & \cdots \\ \hat{\mathrm{V}}_{\mathrm{S},1,\mathrm{Z}} & \hat{\mathrm{V}}_{\mathrm{S},1+\mathrm{N},\mathrm{Z}} & \cdots \end{bmatrix}. \tag{22}$$

Moreover, based on $\widetilde{\mathbf{P}}_{\mathbf{M}}$ and $\widetilde{\mathbf{V}}_{\mathbf{M}}$ of the main satellite, the slant distance R1 between the main satellite and the scene center, Doppler frequency and imaging parameters, the Range-Doppler positioning method [33] is adopted to calculate the position vector of the target as

$$\mathbf{P}_{\mathbf{T}} = \begin{bmatrix} \mathrm{P}_{\mathrm{T},1,\mathrm{X}} & \mathrm{P}_{\mathrm{T},1+\mathrm{N},\mathrm{X}} & \cdots \\ \mathrm{P}_{\mathrm{T},1,\mathrm{Y}} & \mathrm{P}_{\mathrm{T},1+\mathrm{N},\mathrm{Y}} & \cdots \\ \mathrm{P}_{\mathrm{T},1,\mathrm{Z}} & \mathrm{P}_{\mathrm{T},1+\mathrm{N},\mathrm{Z}} & \cdots \end{bmatrix}. \tag{23}$$

According to $\mathbf{P}_{\mathbf{T}}$ and the sampled position vector $\widetilde{\mathbf{P}}_{\mathbf{S}}$ of the slave satellite, the slant distance between the slave satellite, and the target is calculated as

$$\mathbf{R_2} = \sqrt{(\widetilde{\mathbf{P}}_{\mathbf{S,X}} - \mathbf{P}_{\mathbf{T,X}})^2 + (\widetilde{\mathbf{P}}_{\mathbf{S,Y}} - \mathbf{P}_{\mathbf{T,Y}})^2 + (\widetilde{\mathbf{P}}_{\mathbf{S,Z}} - \mathbf{P}_{\mathbf{T,Z}})^2} \tag{24}$$

where $\mathbf{P}_{\mathbf{T,X}}$, $\mathbf{P}_{\mathbf{T,Y}}$, and $\mathbf{P}_{\mathbf{T,Z}}$, respectively, represent the X-, Y-, and Z-axis components of $\mathbf{P}_{\mathbf{T}}$; and $\widetilde{\mathbf{P}}_{\mathbf{S,X}}$, $\widetilde{\mathbf{P}}_{\mathbf{S,Y}}$, and $\widetilde{\mathbf{P}}_{\mathbf{S,Z}}$, respectively, denote the X-, Y-, and Z-axis components of $\widetilde{\mathbf{P}}_{\mathbf{S}}$.

Then, the slant distance difference between the main satellite and the slave satellite is $\mathbf{\Delta R} = \mathbf{R2} - \mathbf{R1}$. The azimuth time of the slave satellite receiving the target echoes can be obtained based on $\mathbf{\Delta R}$, and it is expressed as

$$\overline{\widetilde{\mathbf{T}}}_{\mathbf{S}} = \widetilde{\mathbf{T}}_{\mathbf{S}} + \frac{\mathbf{\Delta R}}{c} = [\hat{\mathrm{t}}_{\mathrm{S},1}, \hat{\mathrm{t}}_{\mathrm{S},1+\mathrm{N}}, \cdots] + \frac{\mathbf{\Delta R}}{c} \tag{25}$$

where c is the speed of light.

Based on $\overline{\widetilde{\mathbf{T}}}_{\mathbf{S}}$, $\mathbf{T}_{\mathbf{S}}$, $\mathbf{P}_{\mathbf{S}}$, and $\mathbf{V}_{\mathbf{S}}$ of the slave satellite, and the high-precision orbit propagator, the position vector, and velocity vector of the slave satellite receiving the target echoes can be derived as

$$\overline{\widetilde{\mathbf{P}}}_{\mathbf{S}} = \begin{bmatrix} \overline{\widetilde{\mathrm{P}}}_{\mathrm{S},1,\mathrm{X}} & \overline{\widetilde{\mathrm{P}}}_{\mathrm{S},1+\mathrm{N},\mathrm{X}} & \cdots \\ \overline{\widetilde{\mathrm{P}}}_{\mathrm{S},1,\mathrm{Y}} & \overline{\widetilde{\mathrm{P}}}_{\mathrm{S},1+\mathrm{N},\mathrm{Y}} & \cdots \\ \overline{\widetilde{\mathrm{P}}}_{\mathrm{S},1,\mathrm{Z}} & \overline{\widetilde{\mathrm{P}}}_{\mathrm{S},1+\mathrm{N},\mathrm{Z}} & \cdots \end{bmatrix} \tag{26}$$

$$\overline{\widetilde{\mathbf{V}}}_{\mathbf{S}} = \begin{bmatrix} \overline{\widetilde{\mathrm{V}}}_{\mathrm{S},1,\mathrm{X}} & \overline{\widetilde{\mathrm{V}}}_{\mathrm{S},1+\mathrm{N},\mathrm{X}} & \cdots \\ \overline{\widetilde{\mathrm{V}}}_{\mathrm{S},1,\mathrm{Y}} & \overline{\widetilde{\mathrm{V}}}_{\mathrm{S},1+\mathrm{N},\mathrm{Y}} & \cdots \\ \overline{\widetilde{\mathrm{V}}}_{\mathrm{S},1,\mathrm{Z}} & \overline{\widetilde{\mathrm{V}}}_{\mathrm{S},1+\mathrm{N},\mathrm{Z}} & \cdots \end{bmatrix}. \tag{27}$$

C. Calculation of Interferometric Baselines

The baseline vector between the main satellite and the slave satellite can be calculated based on $\widetilde{\mathbf{P}}_{\mathbf{M}}$ of the main satellite and $\overline{\widetilde{\mathbf{P}}}_{\mathbf{S}}$ of the slave satellite, and it is represented as

$$\mathbf{B} = \widetilde{\mathbf{P}}_{\mathbf{M}} - \overline{\widetilde{\mathbf{P}}}_{\mathbf{S}}. \tag{28}$$

After that, the track, cross-track, and normal (TCN) coordinate system with the main satellite as the origin is obtained based on the sampled position vector $\widetilde{\mathbf{P}}_{\mathbf{M}}$ and velocity vector $\widetilde{\mathbf{V}}_{\mathbf{M}}$ of the main satellite. The direction vector of the T-axis is $\mathbf{Vec_T} = \widetilde{\mathbf{V}}_{\mathbf{M}}/|\widetilde{\mathbf{V}}_{\mathbf{M}}|$, the direction vector of the N-axis is $\mathbf{Vec_N} = \widetilde{\mathbf{P}}_{\mathbf{M}}/|\widetilde{\mathbf{P}}_{\mathbf{M}}|$, the direction vector of the C-axis is $\mathbf{Vec_C} = \mathbf{Vec_N}$ X $\mathbf{Vec_T}$, where X denotes the cross-product operation. For a detailed description of the TCN coordinate system see [22].

The three components of the baseline vector are calculated based on (28) and the direction vectors of the TCN coordinate system, and they are, respectively, described as

$$\mathbf{T_B} = \frac{\mathbf{Vec_T}^{\mathbf{T}} \cdot \mathbf{B}}{2} \tag{29}$$

$$\mathbf{C_B} = \frac{\mathbf{Vec_C}^{\mathbf{T}} \cdot \mathbf{B}}{2} \tag{30}$$

$$\mathbf{N_B} = \frac{\mathbf{Vec_N}^{\mathbf{T}} \cdot \mathbf{B}}{2} \tag{31}$$

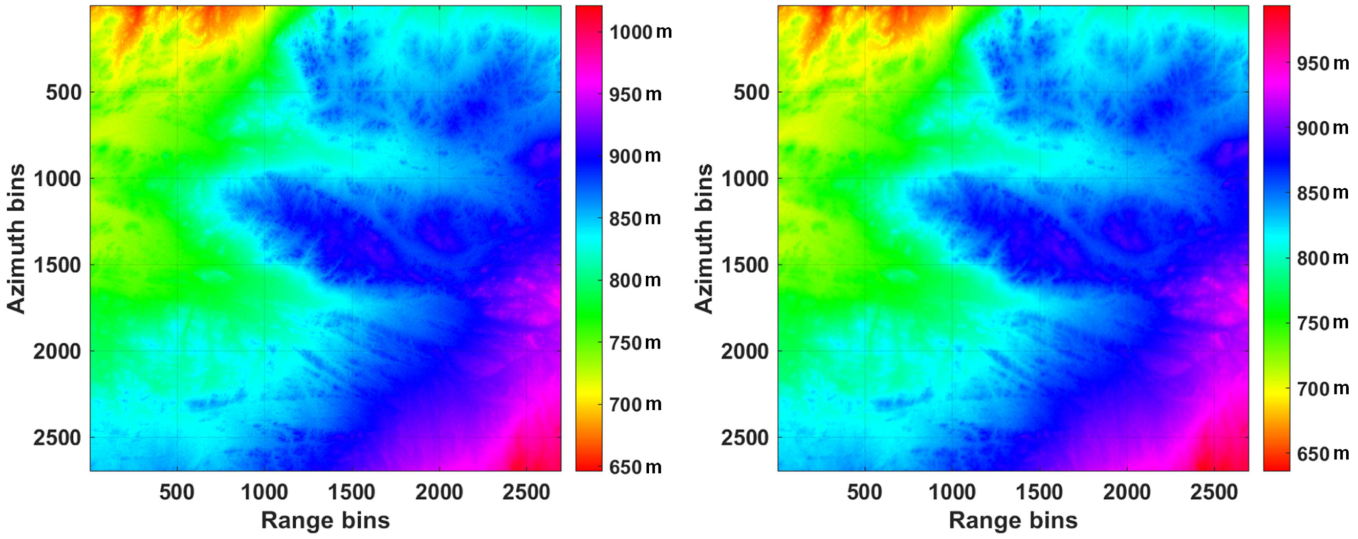

Fig. 5. DEM results of data No. 20220707. (a) DEM of the LT-1 data. (b) the external reference DEM [34].

TABLE III
BASELINE ESTIMATION RESULTS OF DATA NO. 20220707

Compontents	T	C	N
Constant term	-86.5206 m	-968.1914 m	108.9407 m
One-order term	-0.1451 m/s	-0.9339 m/s	-0.0666 m/s

TABLE IV
BASELINE ESTIMATION RESULTS OF DATA NO. 20221019

Compontents	T	C	N
Constant term	-1066.4794 m	-1009.6092 m	500.3766 m
One-order term	-0.9877 m/s	-1.0010 m/s	-0.5739 m/s

where the superscript $\mathbf{T}$ indicates transpose.

It should be noted that the baseline components need to be divided by 2 because the repeat-pass InSAR procedure is used to generate DEM.

Moreover, the quadratic coefficients of (29)–(31) are fitted, respectively, and the constant term and one-order term of the interferometric baseline are obtained. Eventually, based on the estimated interferometric baseline, SLC images, and the procedure in Fig. 3, InSAR processing is performed to obtain high-precision DEM.

Furthermore, two sets of data from the LT-1 system with the high and low orbital parameters are processed for baseline estimation and DEM generation, and the results are compared with the external reference DEM to evaluate the performance of the proposed IBEM and the LT-1 system.

IV. EXPERIMENTAL RESULTS

Based on the state vectors, synchronization signals, and echo data of the LT-1, the IBEM is verified. Because the accuracy of the interferometric baseline directly affects the DEM accuracy, the IBEM can be evaluated by analyzing the DEM accuracy.

The main system parameters of the LT-1 are shown in Table I, and the LT-1, respectively, used two sets of orbital parameters described in Section II-A to perform BiSAR imaging of Hami City, Xinjiang, China, on July 7, 2022, and October 19, 2022. Here, the numbers of these two sets of data are recorded as 20220707 and 20221019, respectively.

First, the time deviation of data No. 20220707 is estimated by the pulse exchange phase synchronization method, and the azimuth time deviation of the slave satellite is compensated. Then, the interferometric baseline of BiSAR is estimated based on Fig. 4, and the results are shown in Table III.

Second, the SLC images of the main satellite multichannel echo and the slave satellite multichannel echo are obtained by interchannel error compensation, multichannel reconstruction, and imaging. Based on the interferometric baseline in Table III, external DEM and the procedure in Fig. 3, image registration, interferogram generation, flat phase removal, phase filtering, phase unwrapping, and absolute phase estimation, conversion of topographic phase to elevation are conducted in sequence to invert the DEM of the target area, and the results are shown in Fig. 5(a).

Furthermore, the DEM in Fig. 5(a) is compared with the reference DEM provided by the SRTM in Fig. 5(b) [34], and the elevation error and statistical results are shown in Fig. 6(a) and (b), respectively. It can be seen from Fig. 6(b) that the standard deviation (STD) of the DEM error is about 3.2 m, which meets the system design requirements of InSAR. It is noted that the system design requirements mainly refer to the relative DEM accuracy of better than 5 m in the article.

Similarly, the data No. 20221019 is processed. According to the procedure in Fig. 4 and satellite orbital parameters, the interferometric baseline is estimated, as shown in Table IV.

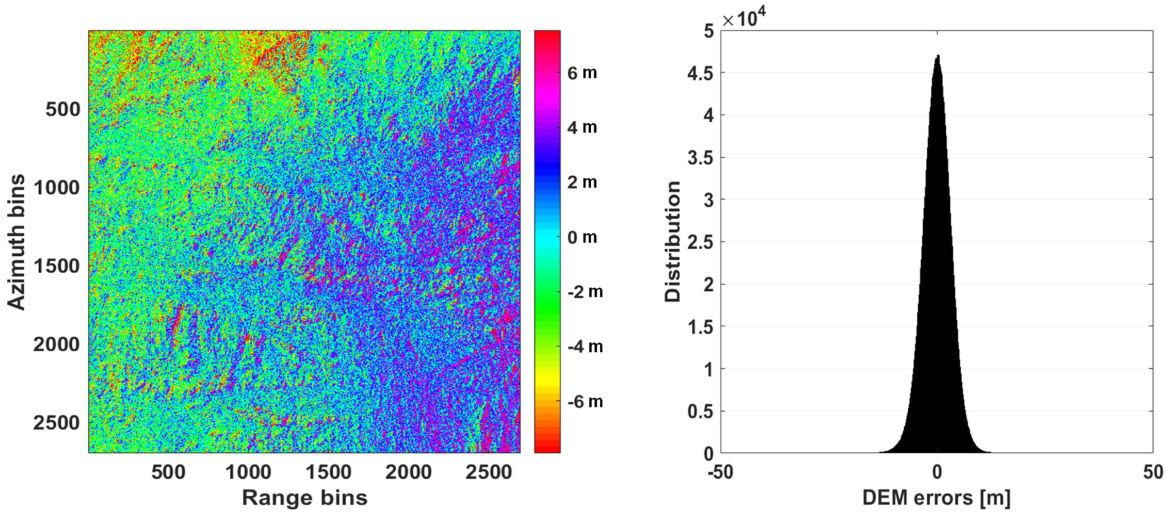

(a) (b)

Fig. 6. Error and statistical results between the DEM of the LT-1 and the external reference DEM in Fig. 5. (a) DEM errors. (b) statistics results.

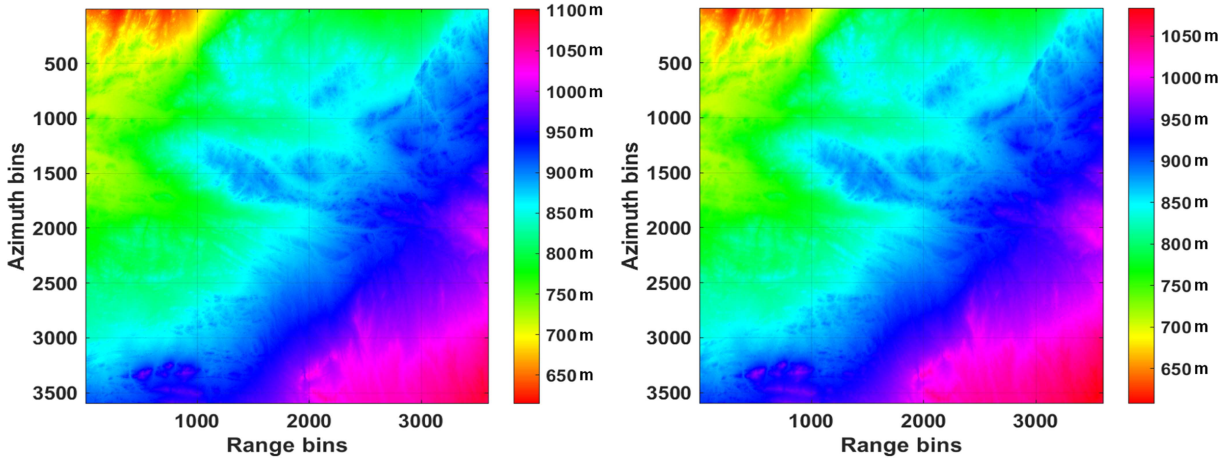

(a) (b)

Fig. 7. DEM results of data No. 20221019. (a) DEM of the LT-1 data. (b) the external reference DEM [34].

Then, the DEM of the target area is generated, as shown in Fig. 7(a). Finally, the DEM in Fig. 7(a) is compared with the reference DEM provided by the SRTM in Fig. 7(b), and the errors and statistical results are obtained, as shown in Fig. 8(a) and (b), respectively. It can be obtained from Fig. 8(b) that the STD of the DEM error is about 2.8 m, which also meets the system design requirements of the LT-1.

In short, these results imply that the accuracy of the DEM acquired by the LT-1 can meet the system design requirements, and the proposed IBEM can accurately estimate the interferometric baseline.

V. Discussion

The DEM accuracy is affected by several factors, including time and phase synchronization, imaging algorithms, internal calibration, external calibration, link errors, and baseline errors. First, radio frequency (RF) interference from communication satellites and radar systems is aliased in synchronization signals, and RF interference suppression should be conducted to improve the accuracy of clock synchronization [10]. Second, the imaging accuracy of BiSAR affects the interferometric phase, and an algorithm with better phase preservation needs to be adopted. Third, internal calibration networks are required to measure and compensate for the errors resulting from temperature variations within the system. Moreover, the internal delay, ionospheric delay, and atmospheric errors of BiSAR affect the interferometric phase, and these errors should be corrected based on the calibration field. In short, there are a lot of factors affecting the DEM accuracy, and most of the errors have been removed for the results in Section IV. To further improve the DEM accuracy, it is necessary to estimate and compensate for these errors more accurately.

The interferometric baseline errors cause the DEM to produce large additional slopes along the range and azimuth directions. Therefore, the interferometric baseline accuracy and the system performance of the LT-1 can be directly evaluated by comparing the generated DEM with the reference DEM obtained based

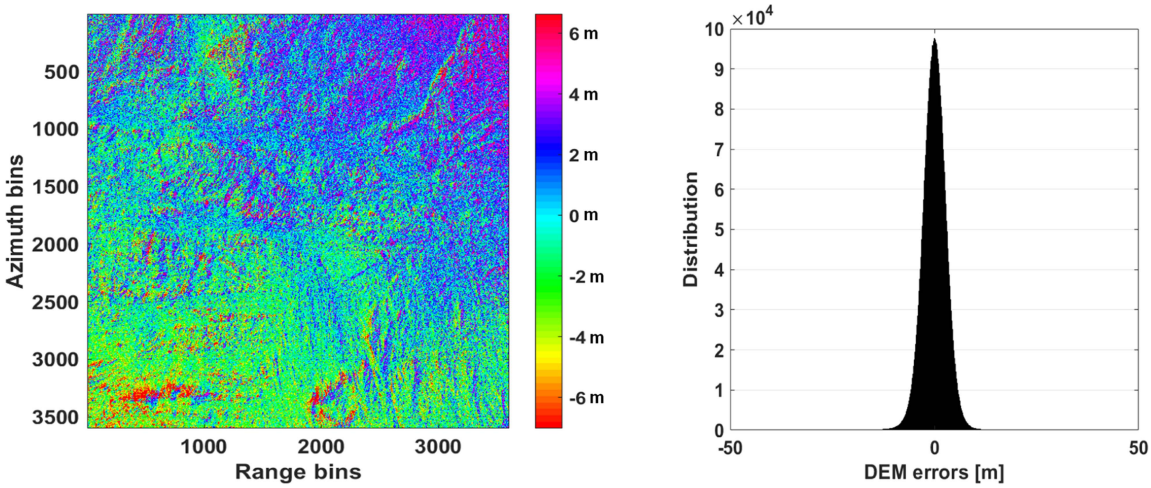

(a) (b)

Fig. 8. Error and statistical results between the DEM of the LT-1 and the external reference DEM in Fig. 7. (a) DEM errors. (b) statistics results.

TABLE V
INTERFEROMETRIC BASELINE ESTIMATION RESULTS BY THE IBEM BASED ON EXTERNAL DEM [22]

Data Number	Components	T	C	N
20220707	Constant term	0 m	-968.1930 m	108.9488 m
	One-order term	0 m/s	-0.9347 m/s	-0.0670 m/s
20221019	Constant term	0 m	-1009.6164 m	500.3833 m
	One-order term	0 m/s	-1.0070 m/s	-0.5735 m/s

on the calibrated baselines. Since the SRTM adopts precisely measured masts to obtain the high-precision baselines, its DEM has eliminated the slopes resulting from baseline errors. To verify the baseline accuracy of the LT-1, the SRTM DEM is an optional reference. Besides, the ICESat-2 and GEDI provide high-precision DEM products, and their poor resolution is not conducive to evaluating the additional slopes of the DEM and the interferometric baseline error. As such, this article adopts the SRTM DEM to evaluate the interferometric baseline accuracy of the LT-1.

In DEM generation, the IBEM based on external data will convert some errors that are not accurately compensated into baseline errors [22], and incorrectly correct the XTI baseline, making it impossible to directly verify the system performance of BiSAR. Fortunately, the IBEM based on satellite orbital parameters avoids this problem, and it is a direct and effective method. As such, this article proposes an advanced IBEM, and it has been verified in the DEM generation of the LT-1 mission. It is noted that the IBEM is also applicable to the TanDEM-X InSAR.

In addition, the IBEM based on external DEM is used here to estimate the interferometric baseline of two groups of data No. 20220707 and 20221019 [22], and the results are shown in Table V. It should be mentioned that the IBEM based on external data mainly estimates the C and N components of the baseline in the TCN coordinate system. Then, the results in Table V are compared with the results in Tables III and IV to further verify the performance of the proposed IBEM. It can be seen that the estimated deviations of the two methods for the C and N components of data No. 20220707 are 1 and 8 mm, respectively, and the estimated deviations of data No. 20221019 are 7 and 7 mm, respectively. In short, the results imply that the proposed IBEM can accurately estimate the interferometric baseline, and the LT-1 has good single-pass XTI performance.

Finally, the issue of the impact of phase unwrapping using the external DEM in Fig. 3 on the final DEM accuracy is clarified. First, the flat and topographic phases are calculated based on the external DEM and removed from the interferometric phase of the LT-1. After that, phase unwrapping is conducted on the obtained interferometric phase with flat and topographic phases removed. Moreover, the flat and topographic phases are added to the unwrapped interferometric phase. In this process, the external DEM is only used to help phase unwrapping, and the phase subtracted before phase unwrapping is added back after phase unwrapping, which does not affect the final DEM accuracy. Thus, the reported results strongly verify the InSAR performance of the LT-1 system.

VI. CONCLUSION

This article puts forward an advanced IBEM and verifies this method in the LT-1 mission. It begins by outlining the satellite formation and DEM generation procedure of the LT-1.

The proposed method is then detailed, covering key aspects including time synchronization deviation compensation, imaging state vector generation, and interferometric baseline calculation. Subsequently, utilizing the method and DEM generation procedures, the article performs interferometric baseline estimation and DEM generation on the LT-1 data. Results demonstrate that the proposed method can accurately estimate the interferometric baseline, emphasizing its potential for promising applications in future spaceborne multibaseline InSAR missions.

ACKNOWLEDGMENT

The authors would like to sincerely thank Professor Irena Hajnsek and Dr. Othmar Frey for providing excellent hardware facilities and enthusiastic help, which supported the successful completion of this paper at the ETH Zürich, Switzerland.

REFERENCES

[1] M. D'Errico, *Distributed Space Missions for Earth System Monitoring*. New York, NY, USA: Springer, 2013.
[2] G. Krieger and A. Moreira, "Spaceborne bi- and multistatic SAR: Potential and challenges," *IEE Proc.-Radar Sonar Navigation*, vol. 153, pp. 184–198, Aug. 2013.
[3] R. Wang and Y. Deng, *Bistatic SAR System and Signal Processing*. New York, NY, USA: Springer, 2018.
[4] A. Moreira, P. Prats-Iraola, M. Younis, G. Krieger, I. Hajnsek, and K. P. Papathanassiou, "A tutorial on synthetic aperture radar," *IEEE Geosci. Remote Sens. Mag.*, vol. 1, no. 1, pp. 6–43, Mar. 2013.
[5] P. Farina, D. Leva, G. Nico, S. Moretti, M. Rinaldi, and D. Tarchi, "Estimating the morphological changes in fluvial beds by means of differential sar interferometry," in *Proc. IEEE Int. Geosci. Remote Sens. Symp.*, 2002, vol. 5, pp. 2924–2926.
[6] Y. Zhang et al., "First demonstration of multipath effects on phase synchronization scheme for LT-1," *IEEE Trans. Geosci. Remote Sens.*, vol. 58, no. 4, pp. 2590–2604, Apr. 2020.
[7] Y. Xia, "Synthetic aperture radar interferometry," *Sci. Geodesy-I, Adv. Future Directions*, pp. 415–474, 2010.
[8] G. Krieger et al., "TanDEM-X: A satellite formation for high-resolution SAR interferometry," *IEEE Trans. Geosci. Remote Sens.*, vol. 45, no. 11, pp. 3317–3341, Nov. 2007.
[9] M. Lachaise, T. Fritz, and R. Bamler, "The dual-baseline phase unwrapping correction framework for the TANDEM-X mission Part 1: Theoretical description and algorithms," *IEEE Trans. Geosci. Remote Sens.*, vol. 56, no. 2, pp. 780–798, Feb. 2018.
[10] Y. Cai et al., "First demonstration of RFI mitigation in the phase synchronization of LT-1 bistatic SAR," *IEEE Trans. Geosci. Remote Sens.*, vol. 61, 2023, Art. no. 5217319.
[11] A. Jones, "China launches 4 InSAR satellites and new Yaogan reconnaissance sat," Mar. 2023. [Online]. Available: https://spacenews.com/china-launches-4-insar-satellites-and-new-yaogan-reconnaissance-sat/
[12] Y. Zhang, H. Zhang, S. Hou, Y. Deng, W. Yu, and R. Wang, "An innovative superpolyhedron (SP) formation for multistatic SAR (M-SAR) interferometry," *IEEE Trans. Geosci. Remote Sens.*, vol. 59, no. 12, pp. 10136–10150, Dec. 2021.
[13] G. Krieger et al., "Mirrorsar: A fractionated space radar for bistatic, multistatic and high-resolution wide-swath SAR imaging," in *Proc. IEEE Int. Geosci. Remote Sens. Symp.*, 2017, pp. 149–152.
[14] P. López-Dekker, H. Rott, P. Prats-Iraola, B. Chapron, K. Scipal, and E. D. Witte, "Harmony: An Earth explorer 10 mission candidate to observe land, ice, and ocean surface dynamics," in *Proc. IEEE Int. Geosci. Remote Sens. Symp.*, 2019, pp. 8381–8384.
[15] Y. Zhang, S. Chang, R. Wang, and Y. Deng, "An innovative push-to-talk (PTT) synchronization scheme for distributed SAR," *IEEE Trans. Geosci. Remote Sens.*, vol. 60, 2022, Art. no. 5213313.
[16] J. Mittermayer et al., "MirrorSAR: An HRWS add-on for single-pass multibaseline SAR interferometry," *IEEE Trans. Geosci. Remote Sens.*, vol. 60, 2022, Art. no. 5224018.
[17] H. Bähr, *Orbital Effects in Spaceborne Synthetic Aperture Radar Interferometry*. Karlsruhe, Germany: KIT Scientific Publishing, 2013.
[18] S. Knedlik, O. Loffeld, A. Hein, and C. Arndt, "A novel approach to accurate baseline estimation," in *Proc. IEEE Int. Geosci. Remote Sens. Symp.*, vol. 1, 1999, pp. 254–256.
[19] K. Singh, N. Stussi, K. L. Keong, and L. Hock, "Baseline estimation in interferometric SAR," in *Proc. IEEE Int. Geosci. Remote Sens. Symp. Proc. Remote Sens.- Sci. Vis. Sustain. Develop.*, 1997, vol. 1, pp. 454–456.
[20] D. Small, C. Werner, and D. Nuesch, "Baseline modelling for ERS-1 SAR interferometry," in *Proc. IEEE Int. Geosci. Remote Sens. Symp.*, 1993, pp. 1204–1206.
[21] H. Kimura and M. Todo, "Baseline estimation using ground points for interferometric SAR," in *Proc. IEEE Int. Geosci. Remote Sens. Symp. Proc. Remote Sens. Sci. Vis. Sustain. Develop.*, vol. 1, 1997, pp. 442–444.
[22] Q. Yang et al., "Image-based baseline correction method for spaceborne InSAR with external DEM," *IEEE Trans. Geosci. Remote Sens.*, vol. 61, 2023, Art. no. 5202216.
[23] J. L. B. Bello et al., "System commanding and performance of TanDEM-X scientific modes," in *Proc. 9th Eur. Conf. Synthetic Aperture Radar*, 2012, pp. 171–174.
[24] Y. Zhang, R. Zhang, R. Wang, and H. Zhang, "The real-time framework of the push-to-talk (PTT) synchronization scheme for distributed SAR," *IEEE Geosci. Remote Sens. Lett.*, vol. 19, 2022, Art. no. 4507705.
[25] D. Liang et al., "The processing framework and experimental verification for the noninterrupted synchronization scheme of LuTan-1," *IEEE Trans. Geosci. Remote Sens.*, vol. 59, no. 7, pp. 5740–5750, Jul. 2021.
[26] H. Zhang and P. Gurfil, "Satellite cluster flight using on-off cyclic control," *Acta Astronautica*, vol. 106, pp. 1–12, 2015.
[27] T. Li, X. Tang, X. Zhou, X. Zhang, S. Li, and X. Gao, "Deformation products of Lutan-1(LT-1) SAR satellite constellation for geohazard monitoring," in *Proc. IEEE Int. Geosci. Remote Sens. Symp.*, 2022, pp. 7543–7546.
[28] W. Zhidong et al., "Identification capability analysis of landslide hazards for LT-1 and sentinel-1 using time series SAR interferometry: A case study of Maoxian, Sichuan," in *Proc. SAR Big Data Era*, 2023, pp. 1–4.
[29] C. Li et al., "Focusing the l-band spaceborne bistatic SAR mission data using a modified RD algorithm," *IEEE Trans. Geosci. Remote Sens.*, vol. 58, no. 1, pp. 294–306, Jan. 2020.
[30] J. Mou et al., "Interferometric calibration and verification in lutan-1 to ensure the global digital elevation quality," in *Proc. 15th Eur. Conf. Synthetic Aperture Radar*, 2024, pp. 1–6.
[31] C. Rossi, F. R. Gonzalez, T. Fritz, N. Yague-Martinez, and M. Eineder, "TanDEM-X calibrated raw DEM generation," *ISPRS J. Photogrammetry Remote Sens.*, vol. 73, pp. 12–20, 2012.
[32] G. Jin et al., "An advanced phase synchronization scheme for LT-1," *IEEE Trans. Geosci. Remote Sens.*, vol. 58, no. 3, pp. 1735–1746, Mar. 2020.
[33] M. Yu, F. Li, Y. Deng, H. Zhang, W. Yu, and R. Wang, "Preliminary analysis of geometric positioning accuracy based on Gaofen-3 data," in *Proc. IEEE Int. Geosci. Remote Sens. Symp.*, 2019, pp. 2937–2940.
[34] T. G. Farr et al., "The shuttle radar topography mission," *Rev. Geophys.*, vol. 45, no. 2, pp. 1–33, 2007.

Yanyan Zhang (Member, IEEE) received the B.S. degree in electronic and information engineering from Hunan University, Changsha, China, in 2017, and the Ph.D. degree in communication and information systems from the University of Chinese Academy of Sciences, Beijing, China, in 2022.

Since 2023, he has been a Postdoctoral Researcher with the Chair of Earth Observation and Remote Sensing, ETH Zürich, Zürich, Switzerland. His research interests include the system design and signal processing of bistatic/multistatic synthetic aperture radar (SAR), SAR tomography technology, and high-resolution wide-swath SAR.

Junfeng Li was born in Henan, China, in 1998. He received the B.S degree from the Department of Electronic Engineering, Tsinghua University, Beijing, China, in 2020. He is currently working toward the Ph.D. degree with the National Key Laboratory of Microwave Imaging Technology, Aerospace Information Research Institue, Chinese Academy of Sciences, Beijing.

He is with the University of Chinese Academy of Sciences, Beijing, China. His research interests include synthetic aperture radar imaging and radio frequency interference suppression.

Pingping Lu (Member, IEEE) was born in Henan, China, in 1989. She received the Ph.D. degree in communication and information systems from the Institute of Electronics, Chinese Academic of Sciences, Beijing, China, in 2016.

She was a Postdoctoral Researcher with the Department of Mechanical Engineering, University of Michigan, Ann Arbor, MI, USA, from 2018 to 2022. She is currently an Associate Research Fellow with the National Key Lab of Microwave Imaging Technology, Aerospace Information Research Institute, Chinese Academy of Sciences, Beijing, China. Her research interests include synthetic aperture radar (SAR) image interpretation, intelligent environment sensing, and deep space exploration.

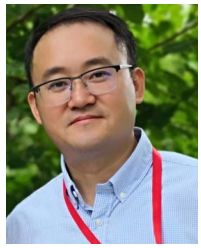

Robert Wang (Senior Member, IEEE) received the B.S. degree in control engineering from the University of Henan, Kaifeng, China, in 2002, and the Dr. Eng. degree from the Graduate University of Chinese Academy of Sciences, Beijing, China, in 2007.

From 2007 to 2011, he was with the Center for Sensor Systems (ZESS), University of Siegen, Siegen, Germany, where he was involved in various joint projects supported by ZESS and Fraunhofer-FHR, Wachtberg, Germany. In 2011, he joined the Aerospace Information Research Institute, Chinese Academy of Sciences (CAS), Beijing, where he is currently the Director of the National Key Laboratory of Microwave Imaging Technology and a Co-Principal Investigator with the Helmholtz-CAS Joint Research Group, Beijing, China. He is the Radar Payload Principal Investigator of the LuTan-1 mission and is responsible for several high-resolution spaceborne imaging radar missions supported by the National High-Resolution Earth Observation Major Special Program. He has authored more than 100 peer-reviewed journal articles and one book. His research interests include mono-/multistatic synthetic aperture radar (SAR) imaging and high-resolution wide-swath spaceborne SAR systems and imaging models.

Dr. Wang currently serves as an Associate Editor for IEEE TRANSACTIONS ON GEOSCIENCE AND REMOTE SENSING.